Energy & Environmental Science

Engineering a Zinc Anode Interphasial Chemistry for Acidic, Alkaline and Non-aqueous Electrolytes

Journal:	*Energy & Environmental Science*
Manuscript ID	EE-ART-01-2024-000062.R1
Article Type:	Paper
Date Submitted by the Author:	18-Feb-2024
Complete List of Authors:	Ma, Lin; The University of North Carolina at Charlotte, Mechanical Engineering & Engineering Science Pollard, Travis; US Army DEVCOM Army Research Laboratory Schroeder, Marshall; US Army DEVCOM Army Research Laboratory Luo, Chao; University of Miami, Department of Chemical, Environmental, and Materials Engineering Zhang, Ye; University of Houston Pastel, Glenn; US Army DEVCOM Army Research Laboratory Cao, Longsheng; University of Maryland at College Park, Chemical and Biomolecular Engineering Zhang, Jiaxun; University System of Maryland, Chemical and Biomolecular Engineering Shipitsyn, Vadim; The University of North Carolina at Charlotte, Mechanical Engineering & Engineering Science Yao, Yan; University of Houston Wang, Chunsheng; University of Maryland at College Park, Chemical and Biomolecular Engineering Borodin, Oleg; US Army DEVCOM Army Research Laboratory Xu, Kang; SES AI,

Amid the global push for eco-friendly and efficient resource utilization, there's a compelling need for alternative battery systems that are able to supplement current Li-ion technologies. Rechargeable zinc metal batteries (RZMBs) present a compelling alternative, capitalizing on significant advantages of zinc anode such as compatibility with aqueous electrolytes, and impressive volumetric and gravimetric capacity (5854 Ah L-1 and 820 mAh g-1). Nevertheless, the widespread adoption of RZMBs encounters challenges associated with electrochemical irreversibility and the suboptimal utilization of zinc metal. These challenges stem from dendritic growth during cycling and side reactions at the electrode–electrolyte interphase. Herein, we present an easily applicable strategy designed to notably improve the cycling performance of zinc metal anodes. This strategy demonstrates effectiveness across various solvent media selections, even at high areal capacities, ensuring 80% utilization of zinc anode. This proposed work hinges on introducing a heteroatomic molecule, specifically 3,5-bis(trifluoromethyl)pyrazole (TFMP). This addition serves to promote a fluorinated and polymeric interphase, thereby facilitating highly reversible Zn chemistry. This study provides novel insights into the deliberate control of zinc anode interphasial chemistries, offering exciting prospects for achieving practical RZMBs.

Engineering a Zinc Anode Interphasial Chemistry for Acidic, Alkaline and Non-aqueous Electrolytes

Lin Ma[a,b,c]§*, Travis P. Pollard[a]§, Marshall A. Schroeder[a]*, Chao Luo[d], Ye Zhang[e], Glenn Pastel[a], Longsheng Cao[f], Jiaxun Zhang[f], Vadim Shipitsyn[b,c], Yan Yao[e], Chunsheng Wang[f], Oleg Borodin[a]*, Kang Xu[a, g]*

a. Battery Sciences Branch, Energy Science Division, Army Research Directorate, DEVCOM Army Research Laboratory, Adelphi, MD 20783, USA

b. Department of Mechanical Engineering and Engineering Science, University of North Carolina at Charlotte, NC 28220 USA

c. Battery Complexity, Autonomous Vehicle and Electrification (BATT CAVE) Research Center, University of North Carolina at Charlotte, NC 28220 USA

d. Department of Chemical, Environmental and Materials Engineering, University of Miami, Coral Gables, FL, 33146, USA

e. Department of Electrical & Computer Engineering and Texas Center for Superconductivity at the University of Houston, University of Houston, Houston, TX 77204, USA

f. Department of Chemical and Biomolecular Engineering, University of Maryland, College Park, MD, USA

g. Current Affiliation: SolidEnergy Systems Corp., Woburn, MA 01801, USA

§ these authors contributed equally

*Corresponding authors: l.ma@charlotte.edu; marshall.a.schroeder.civ@army.mil; oleg.a.borodin.civ@army.mil; kang.xu@ses.ai

Abstract

Reversibility and anode utilization remain key barriers to realizing practical, rechargeable Zn metal batteries. Herein, we report a heteroatomic molecule, 3,5-bis(trifluoromethyl)pyrazole (TFMP), capable of promoting a fluorinated and polymeric interphase in every class of zinc electrolyte (acidic, alkaline, non-aqueous). Significant improvements in performance are observed in TFMP-based electrolytes including Coulombic efficiencies exceeding 99% and utilizations up to 80%. Notably, dendrite formation is effectively suppressed in all classes of electrolytes with the most impressive performance observed in weakly acidic aqueous media with selective entrainers. In full cells constructed with a thin (10-μm) Zn anode and an organic cathode, excellent performance is demonstrated with an exceptionally low n/p ratio (5.4) and high energy density (270 Wh L^{-1}, projected for 18650 cell) in aqueous media. This work highlights that interphasial chemistries

originating from additive-level electrolyte components can manifest major improvements without significantly altering the composition, cost, and key properties of traditional zinc electrolytes that were already optimized.

Main

Lithium-ion batteries (LIBs) are powering an electrification revolution with rapid adoption in electric vehicles, portable electronics, smart-grids and drones. However, given their intrinsic safety and supply chain concerns, the development of complementary battery chemistries is becoming increasingly important.[1-3] Rechargeable batteries based on a zinc metal anode offer a promising complement to LIBs due to key advantages such as compatibility with aqueous electrolytes, high volumetric and gravimetric capacity (5854 Ah L^{-1} and 820 mAh g^{-1}),[4,5] and reduced reliance on critical elements like Co, Ni, and Li.[6] However, practical implementation of rechargeable Zn metal batteries (RZMBs) is still plagued by poor Zn reversibility in plating/stripping and dendrite formation/growth.[7-9]

Compared to artificial interphase engineering[10,11], electrolyte engineering is a proven and economical strategy for tuning both interfacial structures and interphasial chemistries, offering a drop-in approach toward enhancing Zn reversibility without compromising energy density or involving additional processes. The most common approaches are the addition or substitution of a primary component such as a new salt, additive, or co-solvent,[12-17] design of eutectic ionic liquids,[18,19] using polymer electrolytes,[20,21] or formulations intended to modify primary solvent structures[22,23]. Of these approaches, controlling the Zn^{2+} solvation environment has been recognized as the single-most effective method for improving reversibility in aqueous electrolytes. By modifying the Zn^{2+} solvation sheath to contain specific molecules or anions, these electrolytes form a stable interphase on the Zn metal anode. While these research directions have achieved notable progress, certain practical considerations impose limits on this strategy. For instance, the modification of Zn^{2+} solvation sheath in aqueous media often requires high concentrations of expensive salts[24] and co-solvents[25], which will substantially increase the cell-level cost and reduce rate performance. Low salt solubility in organic solvents also restricts the compositional space for electrolyte design[26]. Most importantly, state-of-the-art electrolytes for Zn metal anodes still fail to enable sufficient reversibility under practical loading conditions (5 mAh cm^{-2}, 10 mA cm^{-2}, 80% utilization per cycle) as proposed for lithium metal anodes by Albertus et al.[27,28]. This gap motivates the discovery of new electrolytes with engineered interphase chemistries.

In this work, we reveal how the addition of a fluorinated heteroatomic molecule, 3,5-bistrifluoromethyl pyrazole (TFMP), promotes reversible plating/stripping of Zn metal in all traditional classes of zinc electrolytes, including acidic, alkaline and non-aqueous systems. At only additive-levels (0.05 m) and with low Zn salt concentrations, TFMP enables dendrite-free Zn anodes with CEs above 99% under practical conditions (aqueous: 1.17 mA cm^{-2}, 1.17 mAh cm^{-2}, 20% utilization per cycle; non-aqueous: 9.36 mA cm^{-2}, 4.68 mAh cm^{-2}, 80% utilization per cycle). These performance improvements are ascribed to the polymerization of TFMP on the Zn metal surface, which forms a fluorinated polymer interphase that acts as a protective layer to suppress dendrite propagation and improve reversibility. We also find that this additive can act cooperatively with certain entrainers in aqueous media to further improve deposition uniformity and Coulombic efficiency (CE). Due to TFMP's limited solubility in water, "entrainer" here signifies the addition of non-aqueous chemicals at levels below 1m, serving the purpose of assisted-dissolution of TFMP and ensuring miscibility with aqueous solutions. Compared to other recently reported Zn electrolytes, additive-level amounts of TFMP can support RZMBs with high volumetric energy density and low n/p ratios with high-loading poly(benzoquinonyl sulfide) (PBQS) and polyaniline (PANI) organic cathodes. This work demonstrates a unique and economical approach to electrolyte and interphase engineering for high-performance RZMBs, without significantly altering electrolyte composition or using expensive salts at high concentrations.

Zn metal anode reversibility

Using a galvanostatic protocol with a Cu|Zn (100 μm) cell configuration established in our previous work,[26] we initially examined the performance of electrolytes with TFMP in aqueous (1 m zinc bis(trifluoromethanesulfonyl)imide ($Zn(TFSI)_2$), Figure 1a, S1) and non-aqueous (0.5 m $Zn(TFSI)_2$ in acetonitrile (AN), Figure 1b) media. Without compromising the electrochemical stability of aqueous electrolyte (Figure S1), the average CEs (calculated from Equation 1) of these electrolytes are shown in Figure 1a-b and represent a critical figure-of-merit for the reversibility of the Zn^{2+}/Zn chemistry. Remarkably, the addition of only 0.05 m TFMP in the water and AN-based electrolytes immensely improved the Zn CE up to 95.65% and 99.96%, respectively, as compared to the controls which fail due to parasitic reactions, as in previous work[26]. Interestingly, Zn CE was further improved to 97.39% in aqueous electrolyte with the addition of additive levels of TEP (Figure 1a, S1), suggesting a cooperative effect between TEP and TFMP. TFMP also enhanced Zn reversibility in other common aqueous electrolytes over a wide pH range (Figure S1-2), including mild acidic solutions (pH ~4-6) with $ZnSO_4$, $Zn(OTf)_2$, and alkaline solution (pH ~14) with potassium hydroxide (KOH); however, an additive-level entrainer (e.g. AN, MeOH) was required to dissolve TFMP in these aqueous media at similar concentrations (Figure S3-6). Therefore, acidic, alkaline, and non-aqueous electrolytes with TFMP demonstrate much better reversibility in initial screening experiments with a Cu|Zn (100 μm) cell configuration.

Supporting a high per-cycle Zn utilization is a critical step toward improving the volumetric energy density of RZMBs[28]. Accordingly, we tested these modified baseline electrolytes with a more rigorous "reservoir-free" galvanostatic CE test protocol (Figure S7-8) in a Cu|Zn (10 μm) cell configuration. The 1 m $Zn(TFSI)_2$ + 1 m TEP + 0.05 m TFMP demonstrated stable cycling up to ~50 cycles with a high average CE (98.34%, calculated from Equation 2 for each cycle) and low Zn plating overpotential (~0.1 V) at current density of 1.17 mA cm^{-2}, areal capacity of 1.17 mAh cm^{-2}, and 20% Zn utilization per cycle (Figure 1d), suggesting that interfacial side reactions as well as undesirable morphologies are effectively suppressed. In non-aqueous electrolytes, the addition of 0.05 m TFMP to AN enables extensive cycling (> 600 cycles, 1200h) with a low Zn plating overpotential (< 0.2 V) and high average CE (99.91%, calculated from Equation 2 for each cycle) at 1.17 mA cm^{-2}, 1.17 mAh cm^{-2}, 20% Zn utilization per cycle (Figure 1c). Even more surprisingly, stable cycling (> 160 cycles) with an average CE of 99.9% (calculated from Equation 2 for each cycle) was also achieved at 9.36 mA cm^{-2}, 4.68 mAh cm^{-2}, and 80% Zn utilization per cycle (Figure 1e). In comparison, the non-aqueous control cells failed early on due to the severity of the CE testing protocol (Figure S8). The TFMP electrolytes enable cycling rigorous "reservoir-free" configurations with high utilization and CE with additive-level inclusions of TFMP and TEP entrainer, with TEP entrainer increasing overpotential and presenting a potential trade-off between improvement of CE and overpotential.

To gauge the propensity for dendrite formation and excessive polarization, these electrolytes were also tested in a Zn|Zn (100 μm) symmetric cell configuration under two aggressive galvanostatic conditions: 1 mA cm^{-2}, 1 mAh cm^{-2} per cycle and 2.5 mA cm^{-2}, 2.5 mAh cm^{-2} per cycle for extended durations. In aqueous media, control cells with 1 m $Zn(TFSI)_2$ fail quickly (< 100h, Figure 1f, k) due to excessive polarization. In comparison, the addition of 0.05 m TFMP (Figure 1g, l) or 1 m TEP+0.05 m TFMP (Figure 1h, m) extends the lifetime substantially to ~500 hours (Figure 1g), ~210 hours (Figure 1l), ~3000 hours (Figure 1h), and ~300 hours (Figure 1m), respectively. In non-aqueous media, the addition of 0.05 m TFMP in AN also enhances cycle lifetime by suppressing Zn dendrite formation for ~2500 h at 1 mA cm^{-2}, 1 mAh cm^{-2} (Figure 1j) and ~800 h at 2.5 mA cm^{-2}, 2.5 mAh cm^{-2} (Figure 1o). In contrast, control cells suffer from "soft-short" circuits within a much shorter term (< 200 h) under both loads (Figure 1i, n). According to Li et al.[29], "soft-short" refers to the minor localized electrical link between two electrodes that enables the simultaneous occurrence of direct electron transfer and interfacial reaction. Unlike the common definition of "hard-short", the leakage of electron is not persistent because the pathway established between the electrodes subject to transient fluctuations. Therefore, the interphase enabled by additive-levels of TFMP not only improves CE and utilization, but also helps maintain low dendrite susceptibility and overpotentials.

Postmortem analysis

Analyses using X-ray photoelectron spectroscopy (XPS) depth profiles, focused ion beam-scanning electron microscope (FIB-SEM), transmission electron microscopy (TEM), time of flight secondary ion mass spectrometry (ToF-SIMS) and density functional theory (DFT) calculations reveal the effect of TFMP on Zn electrode morphology and solid electrolyte interphase (SEI) evolution during cycling in both aqueous and non-aqueous electrolytes. Zn samples were recovered from a Zn|Zn (100 μm) symmetric cell configuration after 10 h and 200 h cycling at 0.5 mA cm^{-2} and 0.5 mAh cm^{-2} at room temperature, respectively. Compared to a pristine Zn electrode (Figure S9), the surface morphology of the recovered Zn is no longer flat, with increased surface area even at a very early stage of cycling (10h, Figure 2a, 2f, S10) in aqueous media, most likely due to competition between hydrogen evolution in the mildly acidic aqueous electrolyte (Figure S2) and Zn^{2+}/Zn redox on the electrode. The presence of ZnF_2 signatures (~685 eV) in the F1s spectra (Figure S10) for the aqueous 1 m $Zn(TFSI)_2$ control sample, suggesting decomposition of the TFSI$^-$ anion[30] is counterintuitive because some studies have shown that the TFSI$^-$ anion undergoes a coupled reduction and defluorination at lower potentials.[18,31] ZnF_2 could, however, form either as a result of a high barrier, slow reaction between TFSI$^-$ and OH$^-$,[32] or during reduction of the TFSI$^-$ anion on nano-ZnO clusters (Figure S11), a common component on Zn electrodes. From a kinetic perspective, this process could also be accelerated due to the increased Zn surface area as discussed above. Exposure to the X-ray beam could also contribute to $Zn(TFSI)_2$ salt composition.[33] As for the Zn electrodes cycled in 1 m $Zn(TFSI)_2$+0.05 m TFMP or 1 m $Zn(TFSI)_2$+1 m TEP+0.05 m TFMP aqueous electrolytes, lingering C–F species (~ 688.5 eV) in F1s spectra and a ~293 eV peak in C1s spectra (Figures 2c-e, 2h-j, S10) after 180s of Ar^+ sputtering suggests the formation of TFMP-related interphasial species, which could be the main reason for improved Zn reversibility and will be discussed in detail in the next section. Note that the peak assignment for –CF_3 (~293 eV) and C–S (~286 eV), due to residual TFSI$^-$ anions or its decomposed products, follows previous reports[12,34]. A closer examination of the interphase using TEM shows a ~5 nm SEI layer on the Zn metal surface for TFMP aqueous samples (Figure 2b, 2g), which is also complemented by the F signal in energy-dispersive X-ray spectroscopy (EDX, Figures S12, S13).

After cycling for 200 h, Zn cycled in TFMP-containing electrolytes maintains a homogeneous morphology without dendrite formation (Figures 2k, 2p). By observing C–F species (~ 688.5 eV) in the F1s spectra and a ~293 eV peak in the C1s spectra (Figures 2m-o, 2r-t), the XPS depth profile confirms the remains of SEI chemistries due to TFMP-related reactions even after long-term cycling. Echoing recent reports on implausibly-thick SEI formation in aqueous Zn electrolytes[35,36], the evolution of SEI up to > 1μm in these aqueous electrolytes was observed after 200 h cycling using TEM (Figure 2l, 2q) with EDX confirmation (Figures S14, S15). This is exceptional, especially compared to typical SEI growth on graphite or Li metal anodes in Li-based batteries[37,38]. This suggests that chemical reactions between the aqueous media and Zn electrode could facilitate the growth of thick and permeable interphase regions during long-term cycling; though, the mechanism(s) of Zn-ion conduction in such a thick SEI merits more thorough investigation.

Additionally, the participation of TFMP in the formation of SEI is indicated by the presence of a strong F signal during ToF-SIMS analysis on Zn electrodes obtained from aqueous and non-aqueous electrolytes based on Zn salts with F-free anions (Figure S16). To explore this mechanism, supporting DFT calculations were used to identify potential reaction pathways by which TFMP contributes to Zn interphasial chemistries and is accompanied with experimental results. First, DFT calculations were used to predict the relative binding free energies of different solvates (Figures 3a and S17). While TEP is found to easily displace water from the Zn solvation sheath (Figure S17-18) consistent with prior reports[26], TFMP is not predicted to do so. However, TFMP is predicted to deprotonate on contact with ZnO, OH$^-$ or $[Zn(OH)_4]^{2-}$ (Figure S19). The deprotonated species is an anion $(TFMP_{-H})^-$ and is predicted to be able to displace water from the Zn solvation sheath and has stronger binding than even TEP (Figure 3c). The 2-electron transfer to neutral $Zn(H_2O)_4(TFMP_{-H})_2$ clusters yields a value of 0.91 V (vs. Zn^{2+}/Zn, Figure 3b) in which each $TFMP_{-H}$ defluorinates and the resulting species dimerize across the terminal CF_2 bonds. The products of this reduction exclude water and are likely an initial source of SEI formation at least from a thermodynamic perspective. By contrast, the solvate species produced by 1-electron reduction of $Zn(H_2O)_5(TFMP_{-H})$ (Figure 3c) is less likely to contribute to SEI formation with a reduction potential of -0.26 V (Figure 3c). Therefore, the impressive Zn anode reversibility (Figure 1) is the combination of TEP suppressing dendrites and eliminating soft-shorts[23,39] while TFMP reacts and contributes to SEI formation. It's worth noting, TFMP becomes less effective in a basic environment compared to the mildly acidic environment (Figures S3-4), which could be due to formation of $K(TFMP_{-H})$ with KOH in the bulk instead of reacting locally at the zinc anode surface. To further enhance the reversibility of zinc anodes in more alkaline media, it is encouraged to explore other entrainers that synergize and strengthen the formation of the robust SEI.

Similar postmortem analysis was applied to Zn metal anodes obtained from AN-based non-aqueous electrolytes. Differing from aqueous samples, the Zn morphology grown in the AN remains flat throughout the cycling protocol (Figures 4a, 4f). In the C1s spectra of the control (Figures 4c-e) and TFMP-derived samples (Figures 4h-j), a peak at ~289.5 eV can be detected at the very beginning stages of Ar^+ bombardment, which suggests the presence of a thin, natural layer of carbonaceous species on the Zn surface. Except for this peak, no other peaks can be detected in both C1s and F1s spectra, even after sputtering for 180 s (Figures 4h-j), which rules out the possibility of $TFSI^-$ anion decomposition and is consistent with previous reports[31,40]. With the addition of 0.05 m TFMP, $Zn\underline{F}_2$ and C–$\underline{F}$ signals are detected in F1s spectra after only 10 h of cycling (Figures 4h-j). Correspondingly, a peak at ~293 eV is shown in the C1s spectra (Figures 4h-j), which should be assigned to ($–CF_2–\underline{C}F_2–$) groups according to DFT calculations (Figure 3) and was verified by observation of a ~10 nm SEI layer under TEM (Figure 4g, S20). No such layer is observed on the AN control samples (Figure 4b).

The Zn morphology in the AN-based electrolytes (Figures 4k, 4p) changed dramatically, becoming very rough with increased surface area after cycling for 200 h. Surprisingly, the AN control electrolyte produces a $Zn\underline{F}_2$ peak in the F1s spectra even after sputtering (Figures 4m-o). This likely indicates the decomposition of $TFSI^-$ anions, due to electrochemically active regions of nano-ZnO, as mentioned previously. The addition of TFMP increases the abundance of C–$\underline{F}$ species observed in the F1s spectra after sputtering (Figures 4r-t), which further supports the existence of polymeric species (Figure 3) contributing to the underlying SEI. In sharp contrast to the SEI evolution in aqueous media (Figure 2l, 2q), the SEI thickness (< 20 nm) does not grow substantially in the non-aqueous electrolytes (Figures 4l, 4q, S21) during 200 h of cycling.

Full cell demonstrations

The extraordinary performance of Zn metal in TFMP-based electrolytes suggests significant promise toward practical RZMBs. Pursuing this direction, we selected two transition metal-free organic cathode chemistries to demonstrate the effectiveness of TFMP in both aqueous and non-aqueous electrolytes. RZMBs with excess Zn (100 μm thickness) were prepared for screening purposes while thin (10 μm) and high areal capacity (5.85 mAh cm^{-2}) metal anodes were used in select cells as a rigorous demonstration aimed at commercial viability. PBQS exhibits a non-hydrated Zn^{2+}-ion storage linked to the quinone-related n-type redox reaction, while anions participate to a lesser extent in the reaction through p-dopable thioether linker[41,42]. Meanwhile, PANI predominately participates in the redox process via anion doping mechanism[43]. An initial capacity increase while cycling is observed in all the cases here due to the activation processes reported previously[43,44]. Compared to the control aqueous electrolyte of 1 m $Zn(TFSI)_2$, the addition of 0.05 m TFMP alone shows moderate improvement of capacity retention. The 1 m $Zn(TFSI)_2$ + 0.05 m TFMP + 1 m TEP electrolyte demonstrates superior cycling stability in PBQS|Zn-excess cells with 80% of the maximum capacity retained even after 500 cycles (Figure 5a). Upon optimization of the N/P ratio (the capacity ratio between negative and positive electrode) to 5.4, the aqueous 1 m $Zn(TFSI)_2$ + 0.05 m TFMP + 1 m TEP electrolyte in a PBQS|Zn-thin cells (PBQS: 6 mg cm^{-2}, 1.08 mAh cm^{-2} (estimated using 180 mAh g^{-1}))/Zn (10 μm thickness, 7.14 mg cm^{-2}, 5.85 mAh cm^{-2}) exhibit > 80% retention of the maximum capacity after 70 and 130 cycles, respectively, with a high specific capacity at high rates (400 mA g^{-1} and 800 mA g^{-1}, corresponding to cathode active material mass) between 0.5 V and 1.6 V at 30°C (Figures 5b-c). A high Zn utilization per cycle of 20% and 16% (Figure S22), respectively, was also achieved during such testing at these rates which likely represent the most rigorous RZMB performance to date.

In non-aqueous electrolyte, the addition of 0.05 m TFMP results in better capacity retention after 200 cycles for PANI|Zn-excess cells (Figure 5d), which could partially be attributed to the suppression of parasitic reactions on the Zn anode. The non-aqueous electrolyte also enables PANI|Zn-thin cells with an optimized N/P ratio of 5.4 (PANI: 9 mg cm^{-2}, 1.08 mAh cm^{-2} (estimated using 120 mAh g^{-1}); Zn: 10 μm thickness, 7.14 mg cm^{-2}, 5.85 mAh cm^{-2}), at different rates (40 mA g^{-1} and 480 mA g^{-1}, Figure 5e-f), and with > 80% capacity retention after 300 cycles, corresponding to a Zn utilization per cycle of 19% and 15%, respectively (Figure S22).

To benchmark these results, we extracted the volumetric energy density from the most promising RZMBs described in the literature (Figure S23-24) with a complete discussion outlined in the experimental section and Table S1. By tuning the N/P ratio within our lab to ensure a high cell-level areal capacity and reasonably large fraction Zn utilization per cycle (~20%), this work demonstrates outstanding results among other aqueous and non-aqueous electrolyte efforts using organic cathode chemistries (Figure 5g). Although some pioneering work has demonstrated practical N/P ratios (~1)[25,45], their volumetric energy density is limited due to the bottlenecks related to cathode materials (i.e. specific capacity and average voltage) and the electrode fabrication technique. To realize commercial RZMBs with compelling volumetric energy density, these challenges need to be addressed in parallel with electrolyte engineering.

Conclusions

In this work, we demonstrated the utility of 3,5-bis(trifluoromethyl)pyrazole (TFMP) to form fluorinated polymeric interphase and significantly improve Zn reversibility in acidic, alkaline, and non-aqueous electrolytes. XPS depth profiling, TEM, and DFT calculations confirmed the self-polymerization of TFMP as well as effects from the entrainer (e.g. TEP) which suppress dendritic Zn morphology and interfacial side reactions. Electrolytes based on this additive achieved high Zn plating/stripping CE (> 99%) without dendrite growth, even for 10 μm thick Zn electrodes under aggressive testing conditions (in aqueous:1.17 mA cm^{-2}, 1.17 mAh cm^{-2}, 20% Zn utilization per cycle; in non-aqueous: 9.36 mA cm^{-2}, 4.68 mAh cm^{-2}, 80% Zn utilization per cycle). Notably, Zn transport through the growing interphases observed in this work merits further exploration. Paired with various metal-free organic cathode electrodes, RZMBs with outstanding volumetric energy density were demonstrated in both aqueous (267 Wh L^{-1}) and non-aqueous electrolytes (182 Wh L^{-1}) while achieving ~20% Zn utilization per cycle. However, Zn cathodes with improved specific capacity, higher discharge voltages, and enhanced electronic conductivity are still urgently needed. This work reveals a new class of azole-based additives for engineering the interphasial chemistry in a wide spectrum of electrolyte compositions which holds tremendous potential for future RZMBs. The reversibility of other multivalent metal anodes could also benefit from the incorporation of TFMP, contingent on synchronized improvements in the transport kinetics of working ions.

Methods

Materials

Zinc trifluoromethanesulfonate ($Zn(OTf)_2$, 98%), zinc chloride ($ZnCl_2$, >98%) and zinc sulfate monohydrate ($ZnSO_4 \cdot H_2O$, 99.9%) were purchased from Sigma-Aldrich. Zinc bis(trifluoromethylsulfonyl)imide ($Zn(TFSI)_2$, >99%), 3,5-bis trifluoromethyl pyrazole (TFMP, >98%) was purchased from Tokyo Chemical Industry. Acetonitrile (AN, 99.8%) and triethyl phosphate (TEP, >99.8%) were purchased from Sigma-Aldrich. These two solvents were dried using molecular sieves to ensure a low water content (<10 ppm) before electrolyte preparation. Zn foils with different thickness (10 μm (99.9%) and 100 μm (99.994%)) were purchased from Alfa Aesar.

All the electrolyte solutions were formulated by dissolving Zn salts and additives in de-ionized water (18kΩ) or AN according to different concentrations in an Ar-filled glovebox. All the cathode electrode materials including poly(benzoquinonyl sulfide) (PBQS) and polyaniline (PANI) were synthesized according to previous reports[46,47]. The PBQS or PANI powders, Timical super C45 (MTI), and polytetrafluoroethylene (PTFE, Sigma-Aldrich) were dispersed in anhydrous 2-propanol (99.5%, Sigma-Aldrich) with a mass ratio of 7:2:1. The well-dispersed paste was then coated onto Ti mesh current collector, fully compressed with a rolling machine, and exposed at room temperature for 24h to remove 2-propoanol. The thickness of electrodes was measured using a micrometer (Mitutoyo).

Characterizations

Infrared (IR) spectra were collected for aqueous electrolytes in an attenuated total internal reflection (ATR) geometry using a Nicolet 6700 spectrometer (Thermo Scientific) with a diamond ATR setup. The spectra were the average of 64 scans collected at a resolution of 2 cm^{-1}. The morphology of Zn metal electrodes obtained from Zn|Zn symmetric cells at zero state of charge after cycling with different current densities and areal capacities was studied using a scanning electron microscope (SEM, Hitachi SU-70). X-ray photoelectron spectroscopy (XPS) measurements (PHI Versaprobe III) were conducted on Zn electrodes obtained from Zn|Zn symmetric cells at zero state of charge after cycling with different current densities and areal capacities. Zn electrodes were obtained from cells in an argon filled glovebox, rinsed with anhydrous AN and dried in an antechamber under vacuum overnight, then transferred into XPS system by a sealed vacuum transfer setup. The XPS data was collected by using a combination of survey scan (pass energy 224 eV, step size 0.4 eV) and high-resolution scan (pass energy 55 eV, step size 0.05 eV) during Ar^+ sputtering treatment. The X-ray with a power of 25W was focused to a spot size of 100um. A combination of a low energy Ar-ion flow and an electron neutralizer was used for surface neutralization purpose. Sputtering Ar^+ beam was set as 500 V within a 3mm*3mm region. XPS spectra peak was fitted with 70/30 Gaussian/Lorentzian line shapes on a Shirley background through PHI's Multipak software v. 9.6. All the XPS spectra were shifted relative to the binding energy of 284.8 eV (C1s sp3) to compensate for any surface charging off-set during the measurement. The interphasial morphology and chemistry of Zn electrodes was characterized by a transmission electron microscopy (TEM, JOEL 2100F) with energy-dispersive X-ray spectroscopy (EDX) using Zn electrodes obtained from Zn|Zn symmetric cells at zero state of charge after cycling with different current densities and areal capacities. All the TEM samples were prepared by focused ion beam (FIB, Tescan GAIA). Prior to FIB preparation, a ~100nm carbon layer and a tungsten-containing layer were also coated on the sample surface to protect the intact interphase. The distribution of fluorine at different depths in the cycled Zn electrodes was analyzed using time-of-flight secondary ion mass spectroscopy (ToF-SIMS) attached to a Ga^+ based FIB-SEM (Tescan GAIA3) at an accelerated voltage of 30 kV and 1 nA current.

Electrochemical measurements

The Cu|Zn, Zn|Zn, PBQS|Zn and PANI|Zn cells were examined in 2032-type coin cells consisting of glass fiber (Whatman GF/F) as separator and electrolytes (150 μL per cell). All the cells were prepared in an Ar-filled glovebox and tested using a Maccor charge–discharge unit. Zn plating/stripping Coulombic efficiency (CE) was tested with two types of cell set-up: Cu|Zn (100 μm) and Cu|Zn (10 μm) at room temperature. For the initial screening purpose, Cu|Zn (100 μm) cells were conducted following the protocol proposed by previous report[26]. Cu electrode was conditioned by plating (0.5 mA cm^{-2}, 5 mAh cm^{-2}) and stripping Zn (0.5 V) firstly. Then a Zn reservoir with a capacity of 5 mAh cm^{-2} (Q_t) was deposited on Cu by using 0.5 mA cm^{-2} during the following cycle. Afterwards, Zn was plated and stripped during the following 9 cycles with 0.5 mA cm^{-2}, 1 mAh cm^{-2} (Q_c) in each cycle. A capacity (Q_s) was detected when plated Zn was stripped by charging to 0.5 V in the final step. The average CE is obtained based on Equation 1:

$$CE = \frac{9\mathrm{Qc} + \mathrm{Qs}}{9\mathrm{Qc} + \mathrm{Qt}} \qquad \text{Equation 1}$$

For the purpose of practical application, Cu|Zn (10 μm) cell setup was used for further CE measurement. During each cycle, Zn was plated on Cu electrode by discharging the cell using two conditions: 1.17 mA cm^{-2}, 1.17 mAh cm^{-2} (Q_p, 20% Zn utilization per cycle) or 9.36 mA cm^{-2}, 4.68 mAh cm^{-2} (Q_p, 80% Zn utilization per cycle), then Zn was stripped by charging the cell to 0.5 V (Q_s). CE for each cycle is calculated based on Equation 2:

$CE = \frac{Qs}{Qp}$ Equation 2

Zn|Zn (100 µm) symmetric cell setup was tested using different current densities (0.5, 1 or 2.5 mA cm^{-2}) at room temperature. Each charge/discharge step was set as 1 hour. The leverage of aqueous electrolyte in full cell was applied by using two types of cell set-up: PBQS (~3 mg cm^{-2})|Zn (100 µm) and PBQS (~6 mg cm^{-2})|Zn (10 µm) at 30°C between 0.5 V and 1.6 V with 400 mA g^{-1} and 800 mA g^{-1} (based on PBQS mass), respectively. The leverage of non-aqueous electrolyte in full cell was applied by using another two types of cell set-up: PANI (~5 mg cm^{-2})|Zn (100 µm) and PANI (~9 mg cm^{-2})|Zn (10 µm) at 30°C between 0.4 V and 1.5 V with 40 mA g^{-1} and 480 mA g^{-1} (based on PANI mass), respectively. Electrochemical impedance spectroscopy (EIS) measurements were conducted on Zn|Zn symmetric cells with selected electrolytes before or after 10h and 200h cycling at zero state of charge at 25 °C (0.5 mA cm^{-2}, 0.5 mAh cm^{-2}). All the spectra were collected with ten points per decade from 100 kHz to 10 mHz with a signal amplitude of 10 mV at 25 °C by using a single-channel Gamry Potentiostat (Reference 3000). Electrochemical stability window measurements were conducted with a three electrode Swagelok cell containing stainless steel (SS) as the working electrode, carbon black as the counter electrode and Ag/AgCl as the reference electrode. The measurements were carried out using a single channel Gamry Potentiostat (Reference 3000) with a scan rate of 5mV s^{-1} at room temperature within different voltage ranges: -1 V to 0 V for cathodic region; 0 V to 2 V for anodic region.

Computational methods

General

Unless otherwise mentioned, all density functional theory calculations are performed with Gaussian16 rev. C.02 while input files are created using the atomic simulation environment (ASE)[48,49].

Binding free energies

Many variations of clusters with compositions: $Zn[(H_2O)_xTEP_yTFMP_z]$ and $Zn[(H_2O)_xTEP_y(TFMP\text{-}H)_z]$ where x=(4, 5, 6), y=(0, 1, 2), and z=(0, 1, 2) given the constraint that x+y+z=6, were prepared using the NCI ensemble method in CREST. TFMP-H is the anion of TFMP with the N-H proton removed. Conformer sampling was also performed for the individual molecules as well using a combination of the conformer sampling tools in CREST as well as an in-house script using RDKit[50]. For the cases with multiple TEP, TFMP, or a mix of 1 TEP and 1 TFMP, we explicitly consider cluster generation starting from these molecules placed in the axial and neighboring equatorial positions. The geometries of over 120 different octahedral clusters are optimized at the PCM(acetone)/M05-2X/6-31+G(d,p) level of theory. Binding free energies are computed as,

$$\Delta G_b = G_{XS}^{XS} - G_X^{\circ X} - \sum G_s^s$$

where, ΔG_b is the binding free energy, $G_{XS}^{XS}$is the free energy of the cluster immersed in implicit solvent, $G_X^{\circ X}$is the gas phase free energy of the Zn^{2+} ion, and $\sum G_S^s$is the sum of free energies of the different solvating species immersed in implicit solvent. G_S^s reflects the free energy of isolated TEP, TFMP, or TFMP-H but the average free energy per water from a $(H_2O)_6$ cluster. The resulting binding free energies more closely resemble the solvation free energy of Zn^{2+} as a result[51].

Reduction potentials

Reduction potentials of TFMP-H containing solvates were computed using the Nernst equation for 1 or 2-electron reductions as,

$$E^{red} = -\frac{G(A-) - G(A)}{nF} - 3.68\ \mathrm{V}$$

where, n is the number of electrons in the reduction, F is Faraday's constant, G(A^-) is the free energy of the reduced species, and G(A) is the same free energy used in G_{XS}^{XS} for the species with the largest binding free energy (most negative). The clusters of reduced species were generated by a combination of manual editing using software like Avogadro and automated ensemble generation starting from the hand-edited structure[52]. Single and doubly defluorinated species are considered along with dimerization of the terminal CF_2 groups of adjacent TFMP-H species if appropriate. A value of 3.68 V is used to shift the voltage to the Zn^{2+}/Zn scale using a value of 4.44 V for the absolute value of the standard hydrogen electrode and -0.76 V for the standard reduction potential of Zn^{2+}/Zn. There is no consensus on the exact value of the absolute standard hydrogen electrode potential and it may drift depending on the electrolyte composition. The value of this conversion may be subject to change in the future but is the best we can do today. Any references or comparisons to $TFSI^-$ decomposition outside what is shown here are taken from our previous work[30].

TFMP/TFSI reactivity on ZnO particle

The $(ZnO)_{12}$ nanoparticle was adapted from previous work[53]. As with the other calculations, CREST/xTB was used to sample different adsorption sites and orientations of the TFMP/TFSI, or Zn^{2+}-TFMP. The ZnO nanoparticle was fixed for these calculations. All calculations were performed at the PCM(acetone)/M05-2X/6-31+G(d,p) level of theory. The reduction potential is computed as above while the reaction energy is just the difference in free energies between the product and reactant states.

Acknowledgements

This work was supported by the Joint Center for Energy Storage Research (JCESR), an Energy Innovation Hub funded by Department of Energy, through IAA SN2020957. Dr. Lin Ma at UNC Charlotte acknowledges the support from the Dr. Brad. E. Forch Distinguished Postdoctoral Fellowship and the support by the US National Science Foundation Award No. 2301719. The authors thanks Dr. Jiancun Rao and Dr. Sz-Chian Liou (UMD AIM-Lab) for TEM assistance. Dr. Chao Luo acknowledges the support from the George Mason University Quantum Science &

Engineering Center. Drs. L.M., T.P., M.S., G.P., and O.B. wish to acknowledge the many years of service and leadership of Dr. Kang Xu who has retired from federal service.

Competing interests

This work has been filed as US Patent Application No. 20230223595A1.

References

1 Elshkaki, A., Reck, B. K. & Graedel, T. E. Anthropogenic nickel supply, demand, and associated energy and water use. *Resources, Conservation and Recycling* **125**, 300-307, doi:https://doi.org/10.1016/j.resconrec.2017.07.002 (2017).

2 Campbell, G. A. The cobalt market revisited. *Mineral Economics* **33**, 21-28, doi:10.1007/s13563-019-00173-8 (2020).

3 Tabelin, C. B. *et al.* Towards a low-carbon society: A review of lithium resource availability, challenges and innovations in mining, extraction and recycling, and future perspectives. *Minerals Engineering* **163**, 106743, doi:https://doi.org/10.1016/j.mineng.2020.106743 (2021).

4 Winter, M., Barnett, B. & Xu, K. Before Li Ion Batteries. *Chemical Reviews* **118**, 11433-11456, doi:10.1021/acs.chemrev.8b00422 (2018).

5 Parker, J. F. *et al.* Rechargeable nickel–3D zinc batteries: An energy-dense, safer alternative to lithium-ion. *Science* **356**, 415-418, doi:10.1126/science.aak9991 (2017).

6 Yaroshevsky, A. A. Abundances of chemical elements in the Earth's crust. *Geochemistry International* **44**, 48-55, doi:10.1134/S001670290601006X (2006).

7 Yang, Q. *et al.* Dendrites in Zn-Based Batteries. *Advanced Materials* **32**, 2001854, doi:https://doi.org/10.1002/adma.202001854 (2020).

8 Blanc, L. E., Kundu, D. & Nazar, L. F. Scientific Challenges for the Implementation of Zn-Ion Batteries. *Joule* **4**, 771-799, doi:https://doi.org/10.1016/j.joule.2020.03.002 (2020).

9 Schroeder, M. A., Ma, L., Pastel, G. & Xu, K. The mystery and promise of multivalent metal-ion batteries. *Current Opinion in Electrochemistry* **29**, 100819, doi:https://doi.org/10.1016/j.coelec.2021.100819 (2021).

10 Han, J. *et al.* A Thin and Uniform Fluoride-Based Artificial Interphase for the Zinc Metal Anode Enabling Reversible Zn/MnO2 Batteries. *ACS Energy Letters* **6**, 3063-3071, doi:10.1021/acsenergylett.1c01249 (2021).

11 Li, Y. *et al.* A stable fluoride-based interphase for a long cycle Zn metal anode in an aqueous zinc ion battery. *Journal of Materials Chemistry A* **10**, 14399-14410, doi:10.1039/D2TA03550B (2022).

12 Ma, L. *et al.* Functionalized Phosphonium Cations Enable Zinc Metal Reversibility in Aqueous Electrolytes. *Angewandte Chemie International Edition* **60**, 12438-12445, doi:https://doi.org/10.1002/anie.202017020 (2021).

13 Bayaguud, A., Luo, X., Fu, Y. & Zhu, C. Cationic Surfactant-Type Electrolyte Additive Enables Three-Dimensional Dendrite-Free Zinc Anode for Stable Zinc-Ion Batteries. *ACS Energy Letters* **5**, 3012-3020, doi:10.1021/acsenergylett.0c01792 (2020).

14 Yang, W. *et al.* Hydrated Eutectic Electrolytes with Ligand-Oriented Solvation Shells for Long-Cycling Zinc-Organic Batteries. *Joule* **4**, 1557-1574, doi:https://doi.org/10.1016/j.joule.2020.05.018 (2020).

15 Zhang, C. *et al.* A ZnCl2 water-in-salt electrolyte for a reversible Zn metal anode. *Chemical Communications* **54**, 14097-14099, doi:10.1039/C8CC07730D (2018).

16 Zhang, D. *et al.* Electrodeposition of Zinc in Aqueous Electrolytes Containing High Molecular Weight Polymers. *Macromolecules* **53**, 2694-2701, doi:10.1021/acs.macromol.0c00037 (2020).

17 Li, T. *et al.* Engineering Fluorine-rich Double Protective Layer on Zn Anode for Highly Reversible Aqueous Zinc-ion Batteries. *Angewandte Chemie International Edition* **62**, e202314883, doi:https://doi.org/10.1002/anie.202314883 (2023).

18 Qiu, H. *et al.* Zinc anode-compatible in-situ solid electrolyte interphase via cation solvation modulation. *Nature Communications* **10**, 5374, doi:10.1038/s41467-019-13436-3 (2019).

19 Bayer, M. *et al.* Influence of Water Content on the Surface Morphology of Zinc Deposited from EMImOTf/Water Mixtures. *Journal of The Electrochemical Society* **166**, A909-A914, doi:10.1149/2.0121906jes (2019).

20 Ma, L. *et al.* Liquid-Free All-Solid-State Zinc Batteries and Encapsulation-Free Flexible Batteries Enabled by In Situ Constructed Polymer Electrolyte. *Angewandte Chemie International Edition* **59**, 23836-23844, doi:https://doi.org/10.1002/anie.202011788 (2020).

21 Zhao, S. *et al.* Self-Healing and Anti-CO2 Hydrogels for Flexible Solid-State Zinc-Air Batteries. *ACS Applied Materials & Interfaces* **13**, 12033-12041, doi:10.1021/acsami.1c00012 (2021).

22 Naveed, A. *et al.* A Highly Reversible Zn Anode with Intrinsically Safe Organic Electrolyte for Long-Cycle-Life Batteries. *Advanced Materials* **31**, 1900668, doi:https://doi.org/10.1002/adma.201900668 (2019).

23 Naveed, A., Yang, H., Yang, J., Nuli, Y. & Wang, J. Highly Reversible and Rechargeable Safe Zn Batteries Based on a Triethyl Phosphate Electrolyte. *Angewandte Chemie International Edition* **58**, 2760-2764, doi:https://doi.org/10.1002/anie.201813223 (2019).

24 Wang, F. *et al.* Highly reversible zinc metal anode for aqueous batteries. *Nature Materials* **17**, 543-549, doi:10.1038/s41563-018-0063-z (2018).

25 Li, C. *et al.* Enabling selective zinc-ion intercalation by a eutectic electrolyte for practical anodeless zinc batteries. *Nature Communications* **14**, 3067, doi:10.1038/s41467-023-38460-2 (2023).

26 Ma, L. *et al.* Critical Factors Dictating Reversibility of the Zinc Metal Anode. *ENERGY & ENVIRONMENTAL MATERIALS* **3**, 516-521, doi:https://doi.org/10.1002/eem2.12077 (2020).

27 Albertus, P., Babinec, S., Litzelman, S. & Newman, A. Status and challenges in enabling the lithium metal electrode for high-energy and low-cost rechargeable batteries. *Nature Energy* **3**, 16-21, doi:10.1038/s41560-017-0047-2 (2018).

28 Ma, L. *et al.* Realizing high zinc reversibility in rechargeable batteries. *Nature Energy* **5**, 743-749, doi:10.1038/s41560-020-0674-x (2020).

29 Li, Q., Chen, A., Wang, D., Pei, Z. & Zhi, C. “Soft Shorts” Hidden in Zinc Metal Anode Research. *Joule* **6**, 273-279, doi:https://doi.org/10.1016/j.joule.2021.12.009 (2022).

30 Ma, L. *et al.* Ammonium enables reversible aqueous Zn battery chemistries by tailoring the interphase. *One Earth* **5**, 413-421, doi:https://doi.org/10.1016/j.oneear.2022.03.012 (2022).

31 Suo, L. *et al.* “Water-in-salt” electrolyte enables high-voltage aqueous lithium-ion chemistries. *Science* **350**, 938-943, doi:doi:10.1126/science.aab1595 (2015).

32 Dubouis, N. *et al.* The role of the hydrogen evolution reaction in the solid–electrolyte interphase formation mechanism for “Water-in-Salt” electrolytes. *Energy & Environmental Science* **11**, 3491-3499, doi:10.1039/C8EE02456A (2018).

33 Steinrück, H.-G. *et al.* Interfacial Speciation Determines Interfacial Chemistry: X-ray-Induced Lithium Fluoride Formation from Water-in-salt Electrolytes on Solid Surfaces. *Angewandte Chemie International Edition* **59**, 23180-23187, doi:https://doi.org/10.1002/anie.202007745 (2020).

34 Alvarado, J. *et al.* Bisalt ether electrolytes: a pathway towards lithium metal batteries with Ni-rich cathodes. *Energy & Environmental Science* **12**, 780-794, doi:10.1039/C8EE02601G (2019).

35 Cao, L. *et al.* Fluorinated interphase enables reversible aqueous zinc battery chemistries. *Nature Nanotechnology*, doi:10.1038/s41565-021-00905-4 (2021).

36 Zeng, X. *et al.* Electrolyte Design for In Situ Construction of Highly Zn2+-Conductive Solid Electrolyte Interphase to Enable High-Performance Aqueous Zn-Ion Batteries under Practical Conditions. *Advanced Materials* **33**, 2007416, doi:https://doi.org/10.1002/adma.202007416 (2021).

37 Cao, X. *et al.* Monolithic solid–electrolyte interphases formed in fluorinated orthoformate-based electrolytes minimize Li depletion and pulverization. *Nature Energy* **4**, 796-805, doi:10.1038/s41560-019-0464-5 (2019).

38 Nie, M. *et al.* Role of Solution Structure in Solid Electrolyte Interphase Formation on Graphite with LiPF6 in Propylene Carbonate. *The Journal of Physical Chemistry C* **117**, 25381-25389, doi:10.1021/jp409765w (2013).

39 Liu, S. *et al.* Tuning the Electrolyte Solvation Structure to Suppress Cathode Dissolution, Water Reactivity, and Zn Dendrite Growth in Zinc-Ion Batteries. *Advanced Functional Materials* **31**, 2104281, doi:https://doi.org/10.1002/adfm.202104281 (2021).

40 Etman, A. S., Carboni, M., Sun, J. & Younesi, R. Acetonitrile-Based Electrolytes for Rechargeable Zinc Batteries. *Energy Technology* **8**, 2000358, doi:https://doi.org/10.1002/ente.202000358 (2020).

41 Zhang, Y., Liang, Y., Dong, H., Wang, X. & Yao, Y. Charge Storage Mechanism of a Quinone Polymer Electrode for Zinc-ion Batteries. *Journal of The Electrochemical Society* **167**, 070558, doi:10.1149/1945-7111/ab847a (2020).

42 Zhang, Y., Zhao, L., Liang, Y., Wang, X. & Yao, Y. Effect of electrolyte anions on the cycle life of a polymer electrode in aqueous batteries. *eScience* **2**, 110-115, doi:https://doi.org/10.1016/j.esci.2022.01.002 (2022).

43 Shi, H.-Y., Ye, Y.-J., Liu, K., Song, Y. & Sun, X. A Long-Cycle-Life Self-Doped Polyaniline Cathode for Rechargeable Aqueous Zinc Batteries. *Angewandte Chemie International Edition* **57**, 16359-16363, doi:https://doi.org/10.1002/anie.201808886 (2018).

44 Sun, T. *et al.* Poly(2,5-Dihydroxy-1,4-Benzoquinonyl Sulfide) As an Efficient Cathode for High-Performance Aqueous Zinc–Organic Batteries. *Advanced Functional Materials* **31**, 2010049, doi:https://doi.org/10.1002/adfm.202010049 (2021).

45 Jiang, H. *et al.* Chloride electrolyte enabled practical zinc metal battery with a near-unity Coulombic efficiency. *Nature Sustainability* **6**, 806-815, doi:10.1038/s41893-023-01092-x (2023).

46 Song, Z., Qian, Y., Zhang, T., Otani, M. & Zhou, H. Poly(benzoquinonyl sulfide) as a High-Energy Organic Cathode for Rechargeable Li and Na Batteries. *Advanced Science* **2**, 1500124, doi:https://doi.org/10.1002/advs.201500124 (2015).

47 Wan, F. *et al.* An Aqueous Rechargeable Zinc-Organic Battery with Hybrid Mechanism. *Advanced Functional Materials* **28**, 1804975, doi:https://doi.org/10.1002/adfm.201804975 (2018).

48 Hjorth Larsen, A. *et al.* The atomic simulation environment—a Python library for working with atoms. *Journal of Physics: Condensed Matter* **29**, 273002, doi:10.1088/1361-648X/aa680e (2017).

49 Gaussian 16 Rev. C.01 (Wallingford, C., 2016).
50 rdkit/rdkit: 2022_09_3 (Q3 2022) Release (Release_2022_09_3). (Zenodo.
51 Asthagiri, D., Pratt, L. R., Paulaitis, M. E. & Rempe, S. B. Hydration Structure and Free Energy of Biomolecularly Specific Aqueous Dications, Including Zn2+ and First Transition Row Metals. *Journal of the American Chemical Society* **126**, 1285-1289, doi:10.1021/ja0382967 (2004).
52 Hanwell, M. D. *et al.* Avogadro: an advanced semantic chemical editor, visualization, and analysis platform. *Journal of Cheminformatics* **4**, 17, doi:10.1186/1758-2946-4-17 (2012).
53 Ma, L. *et al.* Highly reversible Zn metal anode enabled by sustainable hydroxyl chemistry. *Proceedings of the National Academy of Sciences* **119**, e2121138119, doi:doi:10.1073/pnas.2121138119 (2022).
54 Betz, J. *et al.* Theoretical versus Practical Energy: A Plea for More Transparency in the Energy Calculation of Different Rechargeable Battery Systems. *Advanced Energy Materials* **9**, 1803170, doi:https://doi.org/10.1002/aenm.201803170 (2019).

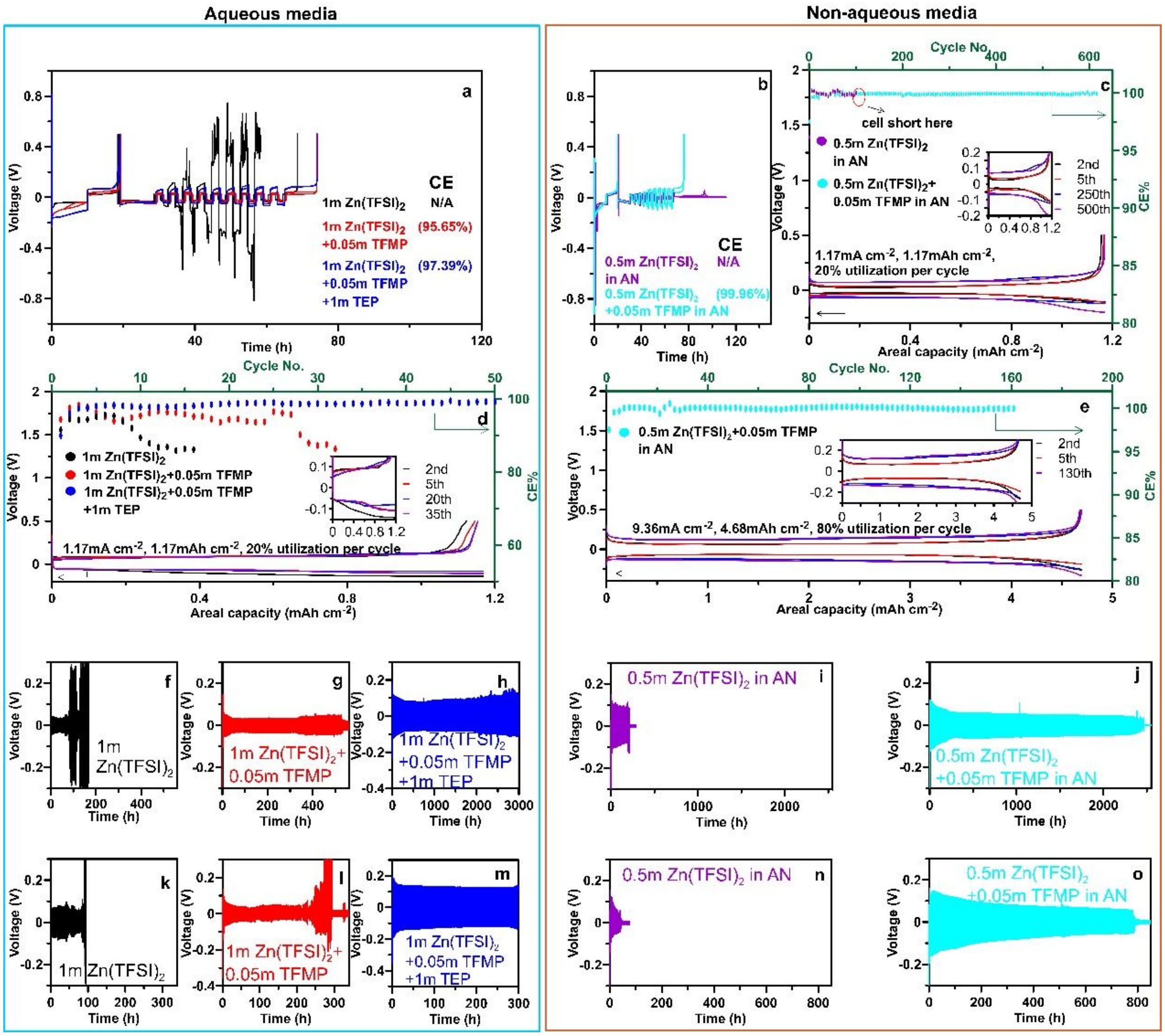

Fig. 1: Zn metal anode reversibility in both aqueous and non-aqueous electrolytes. a,b, Voltage profiles of Cu|Zn (100 μm) asymmetric cells during screening step with aqueous (**a**) or non-aqueous (**b**) electrolytes at room temperature. **c-e,** Zn plating/stripping profiles and corresponding CE cycled using Cu|Zn(10 μm) cell setup at room temperature in aqueous (**d**) or non-aqueous (**c, e**) electrolytes with different testing conditions: 1.17 mA cm^{-2} , 1.17 mAh cm^{-2} per cycle (**c, d**); 9.36 mA cm^{-2} , 4.68 mAh cm^{-2} per cycle (**e**). **f-o,** Voltage profiles of Zn|Zn (100 μm) symmetric cells during long-term cycling in aqueous (**f-h**, **k-m**) or non-aqueous (**i-j, n-o**) electrolytes with different testing conditions: 1 mA cm^{-2}, 1 mAh cm^{-2} per cycle (**f-j**); 2.5 mA cm^{-2}, 2.5 mAh cm^{-2} per cycle (**k-o**) at room temperature.

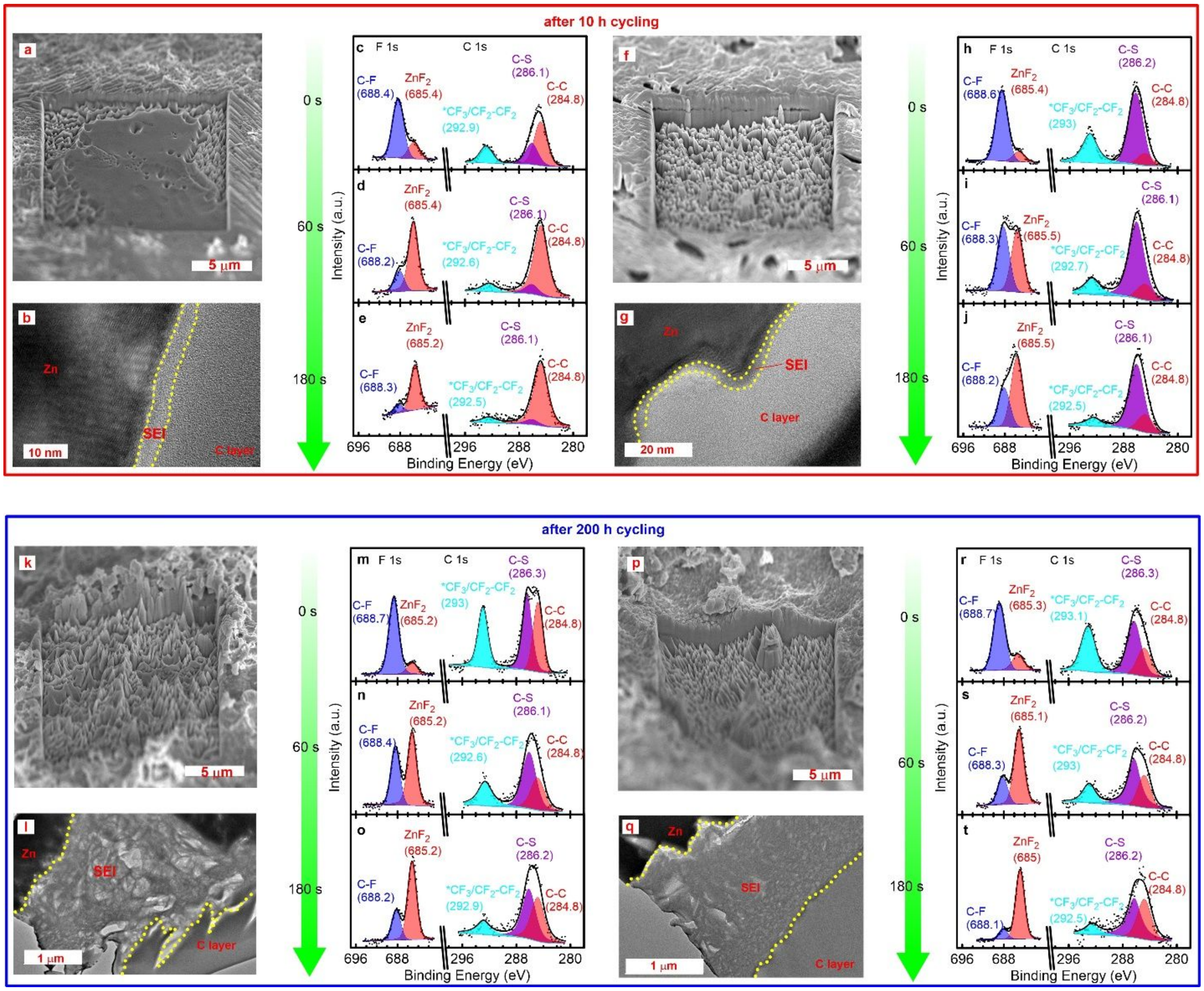

Fig. 2: Zn metal anode morphology and SEI evolution in aqueous electrolytes. a-j, Zn metal anode morphology and SEI information after 10 h cycling (Zn|Zn cell setup, 0.5 mA cm^{-2}, 0.5 mAh cm^{-2} per cycle) at room temperature with different aqueous electrolytes: 1 m $Zn(TFSI)_2$ + 0.05 m TFMP in H_2O (**a-e**); 1 m $Zn(TFSI)_2$ + 1 m TEP + 0.05 m TFMP in H_2O (**f-j**). **k-t,** Zn metal anode morphology and SEI information after 200 h cycling (Zn|Zn cell setup, 0.5 mA cm^{-2}, 0.5 mAh cm^{-2} per cycle) at room temperature with different aqueous electrolytes: 1 m $Zn(TFSI)_2$ + 0.05 m TFMP in H_2O (**k-o**); 1 m $Zn(TFSI)_2$ + 1 m TEP + 0.05 m TFMP in H_2O (**p-t**). Zn morphology was obtained using FIB-SEM (**a**, **f**, **k**, **p**). SEI information was obtained using depth profile XPS (**c-e**, **h-j**, **m-o**, **r-t**) and TEM (**b**, **g**, **l**, **q**).

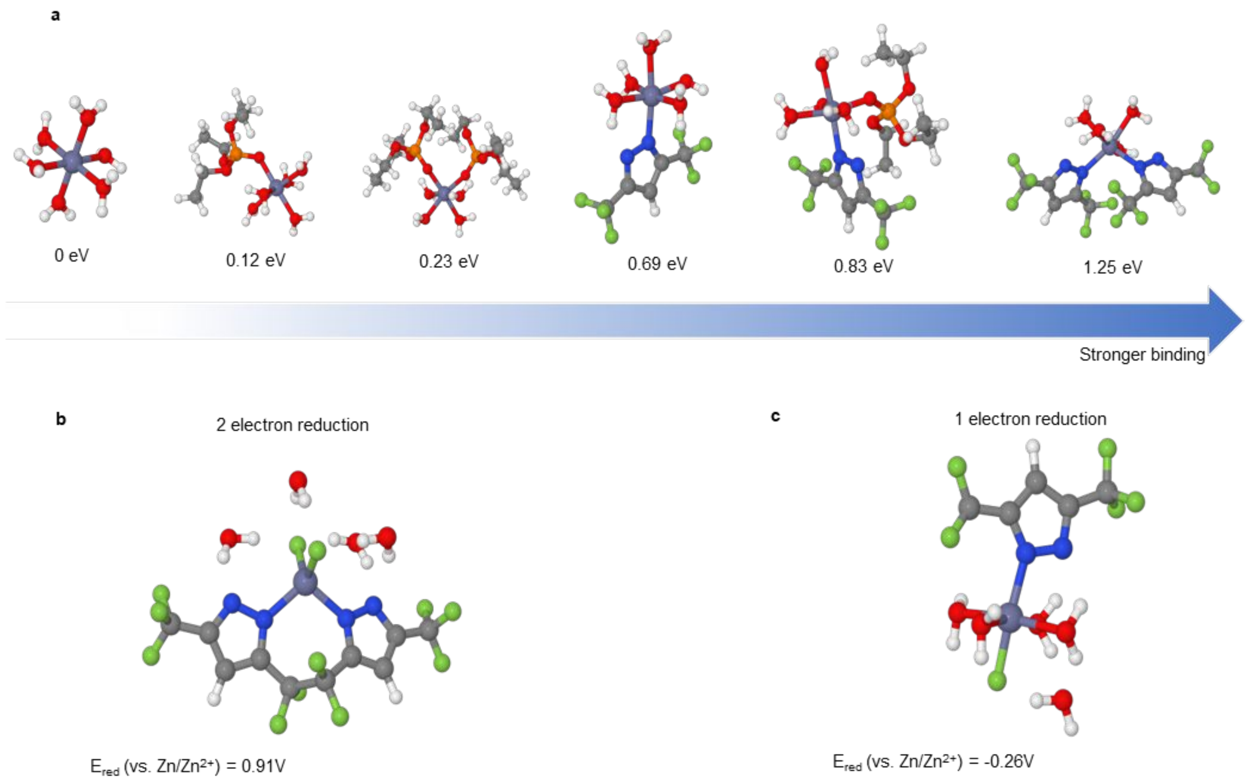

Fig. 3: Proposed SEI formation mechanisms for TFMP. a, Binding free energies from DFT calculations relative to $Zn(H_2O)_6$ in eV for various solvates comprising Zn, H_2O, TEP, and $TFMP_{-H}$; the latter of which is an anion in these solvates. Higher values mean stronger binding. **b-c,** DFT computed double (**d**) and single (**e**) electron reduction potentials of Zn solvates with two or one $TFMP_{-H}$ anions.

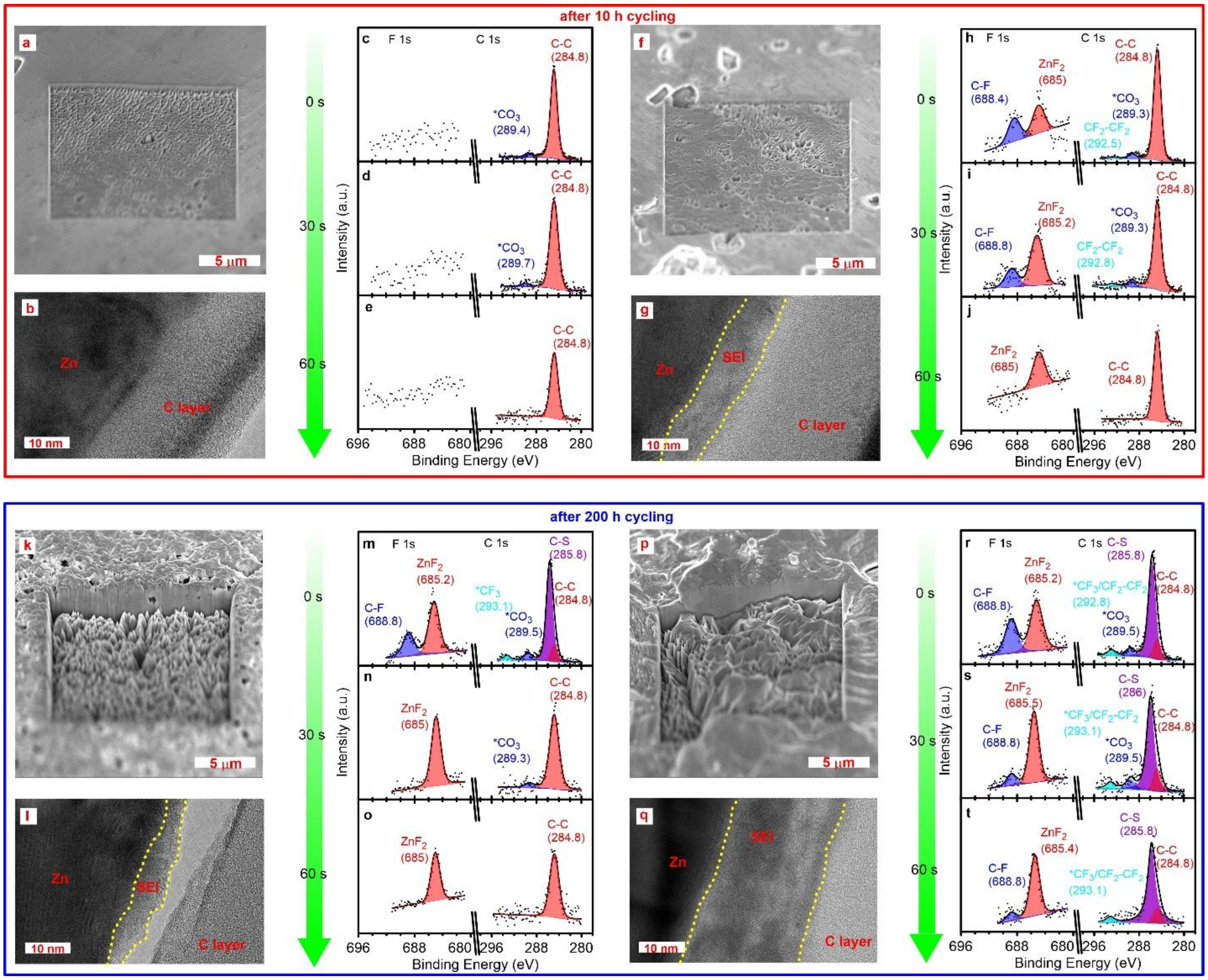

Fig. 4: Zn metal anode morphology and SEI evolution in non-aqueous electrolytes after different periods of cycling including both the 10h and 200h cycles. a-j, Zn metal anode morphology and SEI information after 10 h cycling (Zn|Zn cell setup, 0.5 mA cm^{-2}, 0.5 mAh cm^{-2} per cycle) at room temperature with different non-aqueous electrolytes: 0.5 m $Zn(TFSI)_2$ in AN (**a-e**); 0.5 m $Zn(TFSI)_2$ + 0.05 m TFMP in AN (**f-j**). **k-t,** Zn metal anode morphology and SEI information after 200 h cycling (Zn|Zn cell setup, 0.5 mA cm^{-2}, 0.5 mAh cm^{-2} per cycle) at room temperature with different non-aqueous electrolytes: 0.5 m $Zn(TFSI)_2$ in AN (**k-o**); 0.5 m $Zn(TFSI)_2$ + 0.05 m TFMP in AN (**p-t**). Zn morphology was obtained using FIB-SEM (**a**, **f**, **k**, **p**). SEI information was obtained using depth profile XPS (**c-e**, **h-j**, **m-o**, **r-t**) and TEM (**b**, **g**, **l**, **q**).

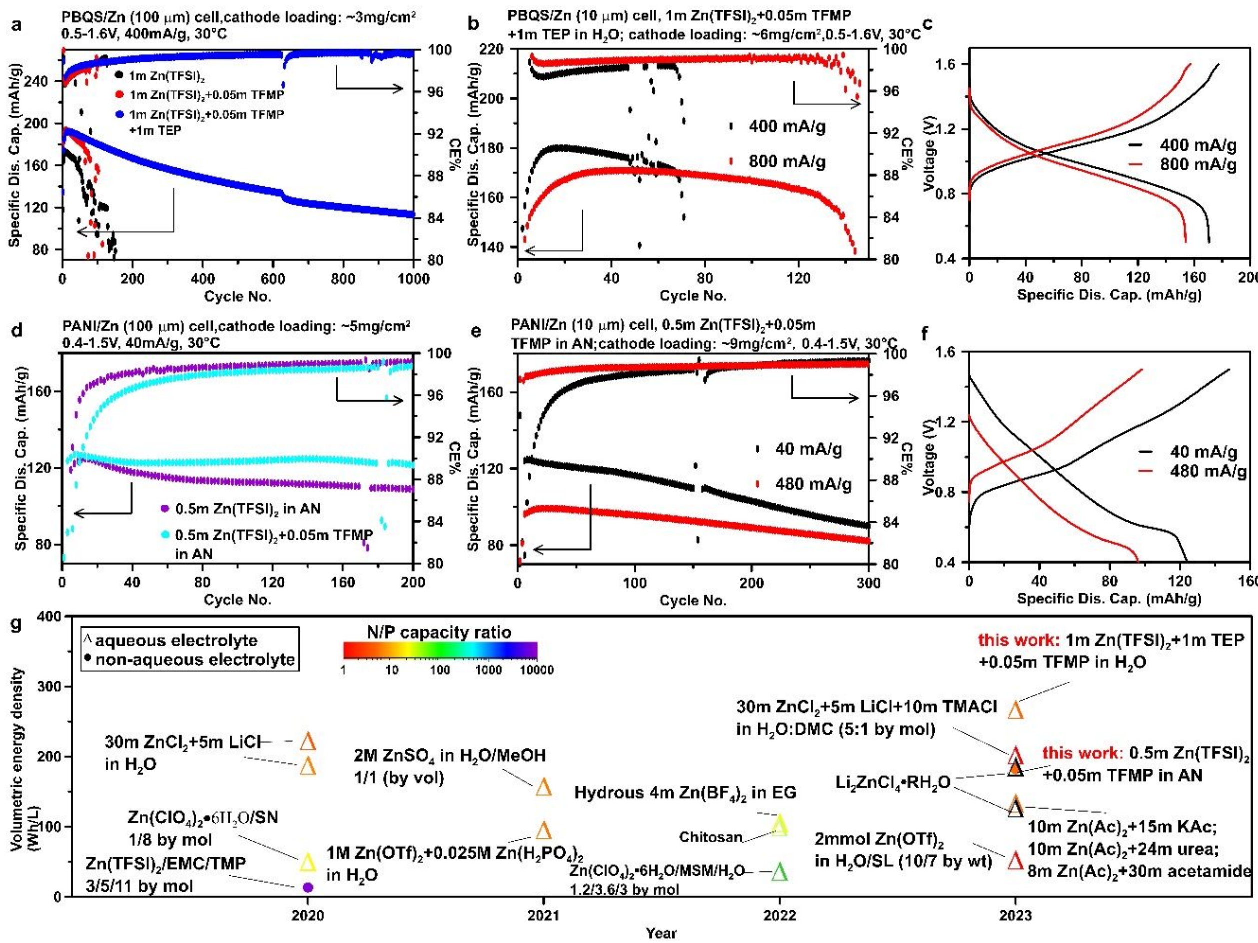

Fig. 5: Zn metal full battery performance. a-c, PBQS|Zn full battery performance (100-µm Zn in **a** and 10-µm Zn in **b, c**) for aqueous electrolytes with CE and corresponding specific discharge capacity vs. cycle number (**a, b**) and charge-discharge profile for 6th cycle after the system stabilizes following the initial activation cycles (**c**) between 0.5 and 1.6 V at 30° C. **d-e,** PANI|Zn full battery performance (100-µm Zn in **d** and 10-µm Zn in **e, f**) for AN-based non-aqueous electrolytes with CE and corresponding specific discharge capacity vs. cycle number (**d, e**) and charge-discharge profile for 6th cycle after the system stabilizes following the initial activation cycles (**f**) between 0.4 and 1.5 V at 30° C. **g,** Cell-level volumetric energy density (only cathode and anode are counted) of selected full cell demonstration on Zn electrolyte efforts by publication year. Calculation was applied based on the 18650-cylinder cell model proposed by Betz et al.[54] using the assumptions outlined in the experimental details